

RETRIEVAL OF THIN ICE THICKNESS
FROM MULTI-FREQUENCY
POLARIMETRIC SAR DATA

R. Kwok, S. V. Nghiem, S. H. Yuch and D. D. Huynh

*Jet Propulsion Laboratory
California Institute of Technology
4800 Oak Grove Drive
Pasadena, CA 91109*

submitted to *Remote Sensing of Environment*

June 15, 1994

Corresponding author:

1 Dr. Ronald Kwok
Jet Propulsion Laboratory
California Institute of Technology
MS 300-235,
4800 Oak Grove Drive
Pasadena, CA 91109

RETRIEVAL OF THIN ICE THICKNESS FROM
MULTIFREQUENCY POLARIMETRIC SAR DATA

R. Kwok, S. V. Nghiem, S. H. Yueh and D. D. Huynh

Jet Propulsion Laboratory

California Institute of Technology

Pasadena, CA 91109

Abstract

We discuss the observed C- and L-band polarimetric signatures of thin lead ice in one Synthetic Aperture Radar (SAR) image based on the expected ice properties and results from a scattering model. In this paper, we focus on thin ice with thicknesses in the range of 0-10 cm. The layered scattering model used here allows for the inclusion of surface and volume scattering contributions from a slush layer, an ice layer and roughness at the interfaces. The sensitivity of the signatures to the model parameters is explored. A highly saline surface skin formed on the top surface during ice growth significantly affects the electromagnetic properties of the medium and helps to explain the magnitude of the co-polarized returns at high incidence angles. Based on these model predictions, we demonstrate an approach to retrieve the ice thickness from polarimetric SAR observations. The approach includes the training of a neural network with model predictions and using this neural network to estimate the ice thickness distribution using polarimetric observations from SAR data. The results from this ice thickness retrieval process are discussed.

1 Introduction

Turbulent heat flux from the ocean to the atmospheric boundary layer is a function of sea ice thickness with an especially strong dependence on sea ice with thicknesses in the 0-100 cm range [Maykut, 1984]. Within this range, the heat flux can increase by at least an order of magnitude as the thickness approaches zero. Even though the area fraction of thin ice is small (2-3%) in the Arctic, the integrated magnitude of flux through this ice can be comparable to that of the thicker ice types. In addition, the brine flux into the ocean is also important due to the growth rate at this thickness range. To date, operational airborne or spaceborne sensors have not been able to provide direct observation of ice thickness. Instead, coarse ice type categories derived from remote sensing data have been used as a proxy indicator of ice thickness. However, it is still difficult to unambiguously discriminate the different types of thin ice from active or passive microwave measurements [Kwok *et al.*, 1992; Cavalieri *et al.*, 1991]. In March 1988, a multi-frequency polarimetric SAR was flown on the NAS ADC-8 aircraft and collected data over Arctic sea ice cover as part of the SSM/I validation campaign. Observations from the polarimetric SAR data indicate that combinations of frequency and polarization enhance our current capability to distinguish ice of different properties [Drinkwater *et al.*, 1991; Kwok *et al.*, 1991]. Rignot and Drinkwater [1993] have evaluated the extraction of ice type from multi-parameter SAR data and discussed the limitation of single-frequency and single-polarization SAR modes for spaceborne SAR sensors. However, the retrieval of ice thickness from polarimetric SAR data have not been addressed mainly due to the lack of coincident surface measurements during the SAR data acquisitions.

Ideally, an ice thickness retrieval process should be based on a theoretical understanding on how the microwave polarimetric signature of thin ice is affected by its physical and electromagnetic properties. Then, an inversion process can be mechanized to estimate the ice thickness from polarimetric observations. In the context of thin ice, very few field measure-

ments of the properties of thin ice are available [Cor and Weeks, 1974; Gow *et al.*, 1990] due to its inaccessibility and fragility in its natural environment. Detailed ice characterization data have been obtained from artificial sea ice grown during the indoor and outdoor Cold Regions Research and Engineering Laboratory Experiments (CRREL/EX) and these experiments have contributed to the pace and understanding of modeling and characterization effort. In this paper, we combine the properties of thin ice available from field and laboratory measurements and a scattering model to explain the polarimetric radar observations. Based on the model results, we explore an approach using neural networks to retrieve ice thickness from the radar measurements. In recent years, neural networks have been applied as non-linear estimators for inversion of multi-dimensional models. Tsang *et al.* [1992] have applied a neural network to invert snow parameters from passive microwave remote sensing measurements. It was pointed out that after the network is trained with input-output pairs generated by scattering models, the computational requirements of the inversion process is very small compared to traditional techniques. Huynh *et al.* [1993] have demonstrated the potential use of neural networks for retrieval of ice thickness from simulated radar data and have studied the robustness of the neural network to speckle. Here, we investigate the application of this technique to real polarimetric measurements.

The following section provides a brief background on polarimetric SAR data and the ice and weather conditions during the acquisition of the data used here. Section 3 focuses on the properties of thin ice, the modeling aspects and comparisons of the model calculations with radar observations. Then, we discuss the approach to ice thickness retrieval and its results in Section 4. The last section summarizes the paper.

2 Data Characteristics and Calibration

2.1 Background

The polarimetric SAR data used here were collected in March 1988 by the NASA/DC-8 multi-frequency polarimetric imaging radar. The radar operates in P, L, and C-band. Each frequency channel has the capability of simultaneously collecting linear like-polarized (HH and VV) and cross-polarized (HV and VH) backscatter data. The transmitter alternately drives the horizontally and vertically polarized antennas while dual receivers simultaneously record the like-polarized and cross-polarized echoes. In this manner, the scattering matrix of every resolution element in an image is measured. The spatial resolution of the 4-look SAR data used here is approximately 6.6 m and 11 m in the slant range and azimuth directions, respectively. The range of look angles is between 20° and 70°.

We define here the polarimetric coefficients used in this paper. Polarimetric backscattering properties of any distributed radar target are described by a covariance matrix, $\overline{\overline{C}}$, containing scattering coefficients defined by,

$$\sigma_{\mu\tau\nu\kappa} = \lim_{\substack{r \rightarrow \infty \\ A \rightarrow \infty}} \frac{4\pi r^2 \langle E_{\mu s} E_{\nu s}^* \rangle}{A \langle E_{\tau i} E_{\kappa i}^* \rangle}$$

where E is the electric field, A is the illuminated area, r is the radar range, the subscripts μ, ν, τ , and κ can be h for horizontal or v for vertical polarization, and the subscripts i and s stand for incident and scattered waves, respectively. The components of the scattered field in the above equation can be obtained by measuring the h and the v polarized returns while the incident field is transmitted exclusively in h or v polarization. For a reciprocal medium, the covariance matrix reduces to,

$$\overline{\overline{C}} = \begin{bmatrix} \sigma_{hhhh} & \sigma_{hhhv} & \sigma_{hhvv} \\ \sigma_{hhhv}^* & \sigma_{hvvv} & \sigma_{hvvv} \\ \sigma_{hhvv} & \sigma_{hvvv}^* & \sigma_{vvvv} \end{bmatrix}$$

where the diagonal elements σ_{hhhh} , σ_{hvvv} , and σ_{vvvv} are the conventional backscattering coefficient σ_{HH} , σ_{HV} , and σ_{VV} , respectively. For sea ice with c-axis having random azimuthal orientation, $\sigma_{hhhv} = \sigma_{hvvv} = 0$ [Nghiem *et al.*, 1992]. Consequently, the covariance matrix contains only five independent parameters: σ_{HH} , σ_{HV} , σ_{VV} , $Re(\sigma_{hhvv})$ and $Im(\sigma_{hhvv})$. Two other frequently used parameters that are derived from these coefficients are,

$$\rho = \frac{<\sigma_{hhvv}>}{\sqrt{<\sigma_{HH}><\sigma_{VV}>}},$$

which is the complex correlation coefficient between the hh and vv channels, and,

$$\gamma = \frac{<\sigma_{VV}>}{<\sigma_{HH}>}$$

is the ratio of the magnitude of the co-polarized returns. The polarimetric SAR scene (CM1372) used in this study is shown in Figure 1. This scene was imaged on March 11 at approximately 1720 GMT. At that time, the scene was located at 73°N and 143° approximately 75-km northwest of the drifting ice station (described below). The color radar image is displayed as a three frequency overlay where the red, green and blue color composites represent the P, L, and C band frequency responses with the pixel intensity modulated by the total backscattered power. In this region, ice conditions comprised of a mixture of first-year (FY) and multiyear (MY) ice forms in this region of transition between the polar pack and younger near shore ice [Drinkwater *et al.*, 1991; Cavalieri *et al.*, 1991]. Visually, the rounded floes which appear as blue are typical of old ice signature (in winter conditions) where the C-band response is dominant. The linear features (yellowish) are ridged or rafted first year ice. The remainder of the image contains first year ice of higher backscatter and the thin ice in the leads which have the lowest backscatter in the scene. It is the ice in these leads which we focus on in this study.

2.2 Weather and Ice drift

Weather and sea ice data were collected in March 1988 within a 150-km radius of the Applied Physics laboratory (APL) drifting ice station (APLIS'88) approximately 350-km north of

Prudhoe Bay, Alaska. Daily air temperatures, atmospheric pressure, wind speed and wind direction were recorded at the location of the ice camp and are reported by *Wen et al.* [1989]. These records provide the most reliable description of the mesoscale meteorological conditions in the region where aircraft remotely sensed data were acquired. Wind speeds on March 11 at the ice camp varied between 1 and 5 m/s from the south due to a low pressure system located over central Alaska. Air temperatures fluctuated between -12°C and -18°C on March 11, while the air temperature of the preceding 4-day period was -16°C.

Ice drift in the location of the scene was observed to be largely westward during the period of observations. Drift speeds recorded at APIS'88 indicated that bouts of rapid ice motion and deformation were correlated with periods of high wind speeds. On the day prior to which the scene was imaged, winds (measured at 3 m height) of approximately 7-8 m/s had been recorded and the sea ice drift peaked at 32 cm/s which was the highest drift speed recorded at APIS'88 during the months of March and April. Divergent ice motion was responsible for many new cracks and leads imaged on March 11 (the SAR data from Figure 1 was collected), and new leads were rapidly freezing under the cold conditions.

2.3 Data Calibration

Polarimetric measurements of all elements in the complex scattering matrix were recorded digitally by the radar. Scattering matrix data are subsequently processed, with proper consideration of polarimetric calibration, into the covariance matrix output described previously. For absolute calibration, σ_{VV} for MY ice is set to be the same backscatter as that observed by C-band VV ERS-1 SAR [*Kwok and Cunningham, 1993*]. At L-band, the absolute scale was set with corner reflectors located near Fairbanks, Alaska. A technique [*Yueh et al., 1992*] which exploits the reciprocity and symmetry of the scattering targets was used for polarimetric calibration. This method calibrates the polarimetric data in amplitude and phase with solutions based on exact relationships for scattering coefficients derived with symmetry

groups and is valid for all scattering mechanisms [Nghiem *et al.*, 1992a]. This method works well for sea ice due to the azimuthal symmetry as a result of the random orientation of the c-axis of the ice crystals.

3 Characterization of Thin Ice

3.1 Thickness of Lead Ice

In this section, we discuss the thickness of the ice in the leads. Although we do not have direct surface measurements of the thickness, the evidence of the thickness range of the ice is given by the weather and ice conditions described above and the almost contemporaneous high resolution passive microwave observation of the same scene during the March 1988 flight campaign. These passive microwave observations were collected by the Naval Research Laboratory (previously NORDA) K_a band scanning radiometer system (KRMS) [Eppler *et al.*, 1986] which was flown on the RP-3A aircraft. On March 11, the passive sensor was flown on the same heading, approximately 10 minutes ahead, as the NASA DC-8 aircraft. Figure 2 shows the KRMS image of the scene, presented with the contrast reversed i.e. the pixel values in the image are inversely proportional to the radiometric brightness of the sea ice. The rounded floes which correspond to multiyear ice have brightness temperatures in the range 01' 165-175°K and the various types of first year ice are radiometrically warmer (darker) than MY ice. The brightness temperature of the lead ice in the scene is between 150-200°K. The variability of the brightness temperature in the 4 leads are shown in Figure 2. We extracted data samples for these four leads from both the SAR and KRMS data. It was observed that nilas (0-10cm) associated with newly frozen leads and bodies of open water span a wide range of brightness temperatures, starting from the brightness temperature of water (145°K), that coincide chiefly with that of old ice to the brightness temperature of first-year ice (220°K) [Eppler *et al.*, 1986]. A direct relationship between the brightness temperature

and ice thickness appears to exist for newly formed ice, such that the brightness temperature increases rapidly with small increases in the ice thickness [Eppler et al., 1986]. However, this relationship was not quantified in their study due to the lack of surface measurements. The brightness temperature of light nilas (5-10 cm) was observed to be over 200°K, which suggests that the ice in the leads is in approximately the same range.

3.2 Ice Properties

Salinity/Brine Inclusions. Field measurements in the Beaufort sea indicate that thin ice with a thickness of a few centimeters can have a salinity as high as 16 parts per thousand [Cox and Weeks, 1974]. For ice less than 0.4 m in thickness, Cox and Winks [1974] have found an empirical linear relationship for the salinity S (in part per thousand - ppt) given by $S = 14.24 - 19.39h$ as a function of thickness h (in meter). This relation suggests salinities of 12.5-14 ppt for the thicknesses (0-10 cm) considered here and we varied the salinities according to this relationship in our model. At an average ice temperature of -8°C [Drinkwater et al., 1991], we calculate the volume fraction of brine inclusion to be 10% based on the equations of Cox and Weeks [1983] with the assumption of no gaseous constituents. In this case, the relative permittivities are $\epsilon_{2s} = 45.3 + 244.8$ [Stogryn and Desargent, 1985] for the brine inclusions and $\epsilon_{2b} = 3.15 + i0.0013$ [Vant et al., 1978; Tiuri et al., 1984] for ice background at C band. At L band, they are $\epsilon_{2s} = 57.3 + i103.0$ [Stogryn and Desargent, 1985] and $\epsilon_{2b} = 2.95 + i0.0014$ [Evans, 1965; Tiuri et al., 1984] for the brine inclusions and ice background, respectively. The ellipsoidal brine inclusions in thin ice are described with correlation lengths of $\ell_{2x'} = \ell_{2y'}/7 = \ell_{2z'}/7.5 = 4.0 \times 10^{-4} \text{ m}$ and with the long axis being vertically aligned or with an orientation probability density $p(\psi, \#J) = \delta(\psi)/(4\pi)$ where ψ and ϕ are the Eulerian angles and δ is the delta function. It has been observed during the Lead Experiment (LEAD EX, 1991 and 1992) that there exists a thin and highly saline surface skim on new ice [Richter-Menge and Perovich, 1992] as a result of brine rejection during ice formation. This surface skim is on the order of millimeters thick composed of ice

and brine with salinity as high as 100ppt. Due to this high salinity, the surface brine layer has a high permittivity and significantly affects the microwave signatures of thin ice. This brine layer was included in our composite scattering model to explain the trends observed in the C- and L-band and polarimetric scattering coefficients. This brine surface skim is assumed to be a mixture of ice and brine with a thickness of 1.2×10^{-3} m and effective permittivities of $\epsilon_{eff} = (12.9 + i9.2)\epsilon_0$ at C band and $\epsilon_{eff} = (15.9 + i21.1)\epsilon_0$ at L band. These are estimated by the Polder and van Santen's mixing formula, which can be reduced from the strong fluctuation results under the low frequency limit [Tsang *et al.*, 1985], for spherical scatterers with fractional volumes of constituents calculated from the salinity in the brine layer. Volume scattering in this thin and lossy layer is ignored in the present model. For sea water, the relative permittivities are obtained from the results of Klein and Swift [1977].

Surface Roughness. At the interface between the air and brine layer, we assume a roughness with a height standard deviation of $\sigma_{01r} = 5.0 \times 10^{-4}$ m and a correlation length of $\ell_{01r} = 0.1$ m while the interface between the brine and ice layers was assumed to be smooth. The underside of the ice layer naturally has some small-scale roughness which has not been well characterized for Arctic thin ice. In the Cold Regions Research and Engineering Laboratory Experiments (CRRELEX), saline ice has been grown in a laboratory environment to simulate thin lead ice. Roughness measurements of the underside of this ice has a height standard deviation σ_{23r} of approximately 4.8×10^{-4} m and correlation length ℓ_{23r} of approximately 8.2×10^{-3} m [Onstott, 1990].

3.3 Model Results

Figure 3 shows physical parameters used in the layered configuration of the scattering model. The predicted C-band and L-band results for a range of thicknesses (1, 3 and 5 cm) are shown in Figure 4. In the model, we vary the thickness of the ice layer. The salinity and brine distributions vary according to the empirical relations discussed in Section 3.2.

These variations result in changes of the ice anisotropic effective permittivity, which affect propagation velocity, attenuation and scattering properties of the sea ice. If the ice layer thickness is assumed to be uniform, the backscattering coefficients oscillate as a function of thickness due to the coherent interference of waves from the layer interfaces. Because sea ice does not have uniform thickness in nature, the information provided by the backscattering coefficients usually represents the average thickness of the ice over a certain range. Hence, we define the ice thickness distribution, $f(h)$, determined by a single parameter gamma distribution:

$$f(h) = \frac{h}{\mu} e^{-h/\mu}$$

where $E(h) = 2\mu$ and μ is the thickness at $\max[f(h)]$. The model results in Figure 4 have been convolved with this distribution function. We note that the backscatter coefficients are less sensitive to changes in thickness at L-band. Figures 5 and 6 compare the model results with actual polarimetric observations. The model results are obtained with the same set of input parameters for C- and L-bands. Radar observations were extracted from the four leads to characterize the incidence angle dependence of the polarimetric parameters. Typically, each data point represents an average of over 50 data samples. We also note here that there could be variability in the ice thickness in the four leads as is evident in the KRMS data, so the incidence angle trend may not be representative of sea ice with an average mean thickness. The superimposed model predictions are from ice with $h = 5$ cm. At C band, σ_{vv} decreases by approximately 5 dB over the range of incidence angles while σ_{hh} has a steeper slope. σ_{vv} is higher than σ_{hh} and the co-polarization ratio γ is small at low incidence and can be larger than 3 dB at high incidence angles. These copolarized returns compare well with the model calculations except that the model calculations are lower at low incidence angles. The cross-polarized returns also compare well although the model calculations are a little higher than the observations. In this model, the cross-polarized returns are caused by the ellipsoidal shape of the scatterers. The magnitude of p at C band is low compared to that observed for first-year and multi-year ice [Drinkwater *et al.*, 1992] and is relatively independent of incidence angles where the observed values of 0.3 to 0.6 are lower than the

calculated values of about 0.65. We attribute this to the low returns from thin ice at C band and the decorrelation effect of noise is more severe [Kwok *et al.*, 1992]. The observed and model calculated phases of ρ are small and show a slightly decreasing trend. At L band, the co-polarized returns σ_{vv} and σ_{hh} decrease quickly as a function of incidence angle and the co-polarized ratios γ are large at high incident angles. The cross-polarized return is a weak function of incidence angle. These conventional backscattering coefficients compare well with the model calculations. In contrast to the behavior of $|\rho|$ measured at C band, $|\rho|$ at L band clearly shows a decrease in magnitude with increasing incidence angles. The phase of ρ at L band is small and a weak function of incidence. Both the magnitude and phase of the complex coefficient ρ compare well with the model results. In general, the calculations from the composite model compare well with the trends observed at both C-band and L-band.

3.4 Discussion of Model Results

For interpretation of the polarimetric backscattering signatures of thin ice, we discuss the scattering mechanisms in the layered configuration used here. If the total scattering is completely due to the volume scattering without surface contribution, the L-band backscattering coefficients σ_{vv} and σ_{hh} are too low especially at low incidence and decrease too slowly with incidence angles in contrast to the experimental observations as seen in Figure 7a. Furthermore, the model calculated $|\rho|$ does not have the strong incidence angle dependence observed in the data as presented in Figure 7b. At L-band, the surface scattering is dominant at small incidence angles, is comparable to the volume scattering at about 30° incidence, and has moderate contribution at larger incidence angles. The surface scattering also contributes to the total scattering at C band but the contribution is smaller for the roughness considered here. On the other hand, surface scattering alone without the volume scattering cannot explain the low values of $|\rho|$ in the observations at both frequencies (Figure 8). The small $|\rho|$'s are due to the decorrelation effect of the ellipsoidal scatterers in an anisotropic layered configuration. Uncorrelated noise in the radar channels can contribute to this decorrelation;

however, an unrealistically large amount of noise in the co-polarized signals is necessary to decrease the $|\rho|$ calculated for surface scattering alone to the level observed in the data. If the scatterers become spherical, the vertical and horizontal returns are more correlated as suggested by the larger $|\rho|$ in Figure 9. Thus, the decrease in $|\rho|$ at L band is due to a combination of the effects of surface roughness and ellipsoidal scatterers. For the highly saline surface skin layer, the effect of the high permittivity enhances the reflection of the energy in the horizontal polarization rather than the vertical. Consequently, the transmission in the horizontal polarization is less, reducing the backscattering coefficient σ_{hh} relative to σ_{vv} , and thus the co-polarized ratio γ becomes larger especially at higher incidence. Without this brine layer, the calculated γ at C band is less than 1 dB at about 50° incidence while the radar measures more than 3 dB. At L band, without this brine layer, the trend in γ is even reversed for model results with $\gamma < 0$ dB while the radar data are about 3 dB at 50° incidence. It seems that the brine layer was important in explaining the observed values of the copolarized ratio γ .

To study the uncertainty due to the correlation lengths of the brine inclusions, a simulation is carried out by varying the correlation lengths by factors of 0.75 and 1.25 (or $\pm 25\%$). The results are presented in Figure 10a for C band and Figure 10b for L band. There are three curves for each of the backscattering coefficient σ_{vv} , σ_{hh} , or σ_{hv} . The middle curve is calculated from the correlation lengths used in the data comparison, the upper is for the 25% increase, and the lower for the 25% decrease. The plots show that the backscattering coefficients at L band, compared to C band, are more sensitive to variations in the correlation lengths which may in turn contribute to the larger fluctuations in the L-band data. Moreover, the copolarized returns σ_{vv} and σ_{hh} at L band have smaller variations at smaller incidence angles as compared to the effect on the cross-polarized return σ_{hv} (Figure 11). The reason is that all the cross-polarized backscattering coefficient is calculated from the ellipsoidal scatterers while the co-polarized returns contain contributions from both volume and surface scattering. L-band returns at smaller incidences are also sensitive to the rough surface

parameters such as the height standard deviation and the surface correlation length. Here, the upper interface dominates the signature so the co-pol returns contain little information about the thickness, especially at low incidence angles.

4 Retrieval of Thin Ice Thickness

4.1 General Approach

A neural network is used as a non-linear estimator for retrieving the mean ice thickness. The approach illustrated in Figure 11. The scattering model described in the preceding section is used to generate the polarimetric scattering coefficients of sea ice with a range of thickness between 0-15cm at the C- and L-band. The five polarimetric coefficients used here are: σ_{HH} , σ_{HV} , σ_{VV} , $Re(\sigma_{hhvv})$, and $Im(\sigma_{hhvv})$. This dataset provide the input-output pairs to ‘train’ the neural network such that the resultant network would provide an estimate of the thickness when presented with a set of polarimetric scattering coefficients. It should be noted here that this is not a direct inversion of a scattering model in the traditional sense. As discussed before, we focus on the lead ice by masking out the thicker ice types using a simple ice type classification scheme described in [Kwok *et al.*, 1992]. The mask for the scene is shown in Figure 1a.

4.2 Neural Network Description/Training

Huynh *et al.* [1993] have investigated the potential application of neural networks (NN) for retrieval of ice thickness by demonstrating the effectiveness of NNs as non-linear estimators when presented with model-generated polarimetric scattering coefficients. Here, we follow the same approach in the design and implementation of the neural network. Briefly, the

neural network consists of an input layer, an output layer and two hidden layers with the nodes in each layer connected to each other. The number of input nodes for the input layer equals the number of input elements. In this case, the inputs are the five polarimetric backscatter coefficients. The number of nodes in the second and third layer are 10 and 30, respectively. There is only one output node, since the average ice properties are functions of ice thickness, which provides an estimate of the thickness of the ice given the polarimetric observations. The backpropagation algorithm described in [Lippmann, 1987] was used for training the network. The algorithm uses the gradient descent method to adjust the connection weights through an iterative process which minimizes the difference between the actual and the desired output of network. After the network is trained, a given training input can be mapped into the desired output with an error rate which is defined by the convergence criteria.

The backscatter coefficients for training the NN were generated by the scattering model described previously. The thickness and salinity are dependent parameters, which have been found to be linearly related to each other as discussed in Section 3. Hence, we relate the salinity (in parts per thousand) given by $S = 14.24 - 19.39h$ with the thickness h in meter. The variations of the ice parameters in the training datasets were discussed in Section 3.3.

In the training dataset, each of the five backscattering coefficients can differ from one another by several orders of magnitude. The effect of this is that, within the network, some coefficients can be weighted more than others. To normalize the inputs, all elements are scaled to between -1 and 1 so that they have the same order of magnitude. Table 1 shows the two sets for incidence angle dependent normalization factors for the L and C-band scattering coefficients. When the NN is used in the estimation mode, these normalization factors are used to scale the input data. Therefore, the relative scaling between the polarimetric radar channels are preserved. We account for the varying polarimetric signature with incidence angle by having separate neural networks at 3 degree intervals, Figure 12 shows the normalized backscattering coefficients versus the average thickness at the two frequencies at the

incidence angle of 40° . The errors in tile estimation of ice thickness after 70,000 iterations through the backpropagation algorithm are shown in Figure 13.

4.3 Retrieval Results

We evaluate our approach at the individual frequencies to estimate average ice thickness as a function of incidence angle since the calibration as well as the scattering coefficients vary as a function of this parameter. Even though there is uncertainty in the actual thickness, we expect the process to provide consistent estimates of the thickness except for the effects of relative calibration between tile frequency channels (which could introduce biases) as well as inefficiencies in the scattering model at C- and L-bands.

During the inversion process, the input polarimetric coefficients to the NN are formed by averaging the polarimetric coefficients of all the lead pixels within a 3° incidence angle range to reduce effect of speckle on the inversion process. We found that speckle introduces a large scatter in our thickness retrieval scheme and since there are very few lead pixels in the image, we resorted to averaging with an incidence angle range. The overall ice thickness distribution of the sea ice in the leads obtained with our retrieval scheme are shown in Figure 15. Within each frequency, the average thickness at each of the the 3° incidence angle interval is shown in Figure 16. The results from the near range incidence angles (less than 35°) are not shown here because some of the radar data are saturated in this range and saturated the network. We do not show the retrieved thicknesses from the L-band data because we do not believe the results to be valid below 40° incidence, we discuss this further below. At both C- and L-bands, the estimated average thickness of the lead ice is between 6-9 cm over the incidence angle range, which shows consistency in the process. We base the following discussion of the results on Figures 16 and 17. We attempt to point out some of the salient points with the realization that this is a demonstration of a process using one dataset and that an in-depth analysis is only justified for a larger dataset has been analyzed.

First, we discuss the discrepancy between the shape of the thickness distribution between L-band and C-band. The L-band distribution terminates more abruptly than the C-band. We noted in Section 3 (Figure 4) that the sensitivity of the L-band signatures to increasing thickness decrease rapidly when the ice is more than 5 cm thick. At L-band, surface scatter dominates (Figure 4) except for higher incidence angles. As a result, the L-band retrievals would saturate beyond a certain thickness which seems to be indicated by the distribution.

Next, we discuss why the lower incidence angle (less than 35°) thickness retrievals are invalid. We attribute the failure of the process to inefficiencies in our model predictions and deficiencies in our retrieval process. At lower incidence angles, the model outputs do not match the polarimetric observations as well, especially at C-band. The lower incidence angle surface scatter contribution at the C-band wavelength is probably not well-modeled with our current set of physical parameters and hence we obtain discrepancies in the calculated and observed results at C-band. Additionally, higher order scattering may have more contribution at C-band. We attribute the poor retrievals results from the L-band to the behavior of thin ice signature as well as the behavior of the retrieval process (Figures 6 and 12). In our scheme, each polarimetric coefficient is normalized independently of each other. We have not taken into account the signal-to-noise ratio of each measurement, the effect of which is to confuse noisy signals as significant discriminators in our process. This is the case at L-band, where the retrieval process is more dependent on the polarimetric coefficients $\ln(HHVV^*)$ and HV , both of which are close to the noise floor of the radar. In contrast, C-band has significant cross-pol(HV) returns due to volume scattering and therefore the retrieval process is more sensitive to the co-polarized responses. This may bias the retrieval process to better performance at C-band. We also examined the sensitivity of the retrieved thicknesses due to calibration errors to evaluate the robustness of the process. The results from biasing the input data by $\pm 1\text{dB}$ is shown in Figure 17. The effect is indeed small.

5 Summary

We have summarized the ice properties of thin sea ice in the 0-10cm range. These properties were used in a scattering model to explain the polarimetric signature of thin ice acquired by the NASA/DC-8 radar. The thickness of the thin ice in the leads is supported by passive observations from the KRMS sensor. The layered scattering model we used here was configured with a surface skim layer and an ice layer on top of a half space of sea water. The surface roughness between the interfaces as well as the volume scatterers in the ice layer were modeled. Comparison of the polarimetric observations with model output showed that, in broad terms, the model calculation predicts the signature of thin ice quite well especially in the incidence angle range between 35° and 45° . We note here that there is probably a mixture of thin ice with different thickness in the leads and as such we do not have the pure signature of a lead with uniform average thickness. We attribute some of the discrepancies we observe between the model calculations and radar measurements to these thickness variations. The significance of the highly saline surface skim layer on the polarimetric signature was pointed out. Its effect on the magnitude of the co-polarized ratio at high incidence angles is an important signature and discriminator for thin ice. Based on these model results, we demonstrated an approach to retrieve thin ice thickness from polarimetric SAR data. An important step in the approach is to mask out the thicker ice types such that the retrieval process can focus on thin lead ice within a limited range of thickness and signature characteristics. The inversion process was mechanized with a neural network trained with a range of input (polarimetric coefficients)-output (ice thickness) characteristics. The stabilized network can then speedily retrieve ice thickness when presented with polarimetric observations. The results and model predictions seem to indicate that C-band performs best in the thickness range 0-10cm due to the scale of the thickness to the wavelength and the corresponding physical and electromagnetic properties of sea ice. The L-band model calculations seem to indicate that the polarimetric measurement would be less sensitive to ice thickness at the range (0-10cm). We have not investigated the contribution of the individual polarization

coefficients to the retrieval process. We plan to further our investigations with polarimetric scatterometer measurements and well-characterized ice properties from future field experiments and laboratory measurements at Cold Regions Research and Engineering Laboratory (CRREL).

Acknowledgment

This work was carried out at the Jet Propulsion Laboratory, California Institute of Technology under contract with the National Aeronautics and Space Administration.

References

- Cavalieri, D.J., J. Crawford, M. R. Drinkwater, D.T. Eppler, L. D. Farmer, R. R. Jentz and C. Q. Wackerman. Aircraft active and passive microwave validation of sea ice concentration from the DMSP SSM/I, *J. Geophys. Res.*, 96(C12), 21989 -2200S, 1991.
- Cox, G.F. N., and W.F. Weeks, Salinity variations in sea ice, *J. Glaciol.*, 13(67), 109-120, 1974.
- Cox, G. F. N., and W. F. Weeks, Equations for determining the gas and brine volumes in sea-ice samples, *J. Glaciol.*, 29(12), 306-316, 1983.
- Drinkwater, M., R. Kwok and D. Winebrenner. Multi-frequency Polarimetric SAR Observations of Sea Ice, *J. Geophys. Res.*, 96(C11), 20679-20698, 1991.
- Eppler, D. T., L. D. Farmer and A.W. Lohanick and M. Hoover. Classification of Sea Ice Types With Single Band (33.6 GHz) Airborne Passive Microwave Imagery. *J. Geophys. Res.*, 91(C9) 10661-10695, 1986.
- Evans, S. , Dielectric properties of ice and snow -- A review, *J. Glaciol.*, 5, 773-792, 1965.
- Gow, A. J., D. A. Meese, D.K. Perovich and W.B. Tucker III, The anatomy of a freezing lead, *J. Geophys. Res.*, , 95(C10), 18221 -18232, 1990.
- Gow, A. J., S. A. Arcone, and S. G. McGrew, Microwave and structure properties of saline ice, *Rep.* 87-20, U. S. Army Corps of Engineers, Cold Regions Research and Engineering Laboratory, Hanover, N.H., 1987.
- Klein, L. A., and C. Swift, An improved model for the dielectric constant of sea water at microwave frequencies, *IEEE Trans. Antennas Propagat.*, AP-25(1), 104-111, 1977.
- Kwok, R., M. R. Drinkwater, A. Pang, and F. Rignot, Characterization and classification of sea ice on polarimetric SAR data, *International Geoscience and Remote Sensing Symposium*, Vol. 11, pp. 81-84, May 26-29, 1991.

- Gray, A. I., R. K. Hawkins, C. E. Livingston, I. 1). Arsenault and W. M. Johnstone. Simultaneous Scatterometer and Radiometer Measurements of Sea-Ice Microwave Signatures. *IEEE J. of Oceanic Engr.*, OK-7(1), 20-32, 1982.
- Huynh, D., S. Yuch, S. Nghiem and R. Kwok, Application of neural network for retrieving sea ice thickness from model-generated polarimetric scattering coefficients. *IEEE Trans. Geosci. Remote Sens.*, , submitted.
- Kwok, R., F. Rignot, B. Holt and R. G. Onstott. Identification of Sea Ice Type in Spaceborne SAR Data. *J. Geophys. Res.*, 97(C2), 2391-2402, 1992.
- Lippmann, R. P., Introduction to Computing with Neural Nets, *IEEE Trans. Acoust. Speech Signal Process*, 4-22, April 1987.
- Livingstone, C. E., K. P. Singh, and A. I. Gray, Seasonal and regional variations of active/passive microwave signatures of sea ice, *IEEE Trans. Geosci. Remote Sens.*, GE-25(2), 159-173, 1987b.
- Maykut, G. A., Energy exchange over young sea ice in the central arctic, *J. Geophys. Res.*, 83(C7), 3646 -3655, 1978.
- Nghiem, S. V., M. Borgeaud, J. A. Kong, and R. T. Shin, Polarimetric remote sensing of geophysical media with layer random medium model, *Progress in Electromagnetics Research*, vol. 3: *Polarimetric Remote Sensing*, Chap. 1, ed. by J. A. Kong, pp.1-73, Elsevier, New York, 1990.
- Nghiem, S. V., S. H. Yuch, R. Kwok, and F. K. Li, Symmetry properties in polarimetric remote sensing, *Radio Sci.*, , 27(5), 693-711, 1992.
- Nghiem, S. V., R. Kwok, J. A. Kong, and R. '1'. Shin, A model with ellipsoidal scatterers for polarimetric remote sensing of anisotropic layered media, *Radio Sci.*, 28(5), 687-703, 1993a.

- Nghiem, S. V., T. Le Toan, J. A. Kong, H.C.Han, and M.Borgeaud, Layer model with random spheroidal scatterers for remote sensing of vegetation canopy, *J. Electromagn. Waves Appl.*, 7(1), 49-76, 1993b.
- Onstott, R.G., Polarimetric radar measurements of artificial sea ice during CRREL-EX'88, *Tech. Rep. 196100-23-T*, Environmental Research Institute of Michigan, Ann Arbor, 1990.
- Richter-Menge, J. A., and D. K. Perovich, Surface characteristics of lead ice, *Supplement to EOS, Transactions, American Geophysical Union*, 73(43), 290, Oct. 1992.
- Rignot, E. and M. Drinkwater, Winter sea ice mapping from multi-parameter synthetic aperture radar. *J. of Glaciology*, submitted.
- Stogryn, A., and G. J. Desargant, The dielectric properties of brine in sea ice at microwave frequencies, *IEEE Transactions on Antennas and Propagation*, AP-33(5), 523-532, May 1985.
- Tiuri, M. E., A. H. Sihvola, E. G. Nyfors, and M. T. Hallikainen, The complex dielectric constant of snow at microwave frequencies, *IEEE Journal of Ocean Engineering*, OE-9(5), 377-382, December 1984.
- Tsang, L., Z. Chen, S. Oh, R. J. Marks II and A. T. C. Chang, Inversion of snow parameters from passive microwave measurements by a neural network trained with a multiple scattering model. *IEEE Trans. Geosci. Remote Sens.*, GE-30(5), September, 1992.
- Tsang, L., and J. A. Kong, Scattering of electromagnetic waves from random media with strong permittivity fluctuations, *Radio Science*, 16(3), 303-320, May-June 1981.
- Tsang, L., J. A. Kong, and R. T. Shin, *Theory of Microwave Remote Sensing*, John Wiley, New-York, 1985.
- Weeks, W. F. and S. F. Ackley, *The growth, structure, and properties of sea ice*, US Army Corps of Engineers CRREL Monograph 82-1, 130 pp., 1982.

Wen, T., W. J. Felton, J. C. Luby, W. L. J. Fox, and K. I. Kientz, Environmental measurements in the Beaufort Sea, Spring 1988, *Applied Physics Laboratory Technical Report* ALP-UW TR 8822, University of Washington, 1989.

Winebrenner, D. P., L. Tsang, B. Wen, and R. West, Sea-ice characterization measurements needed for testing of microwave remote sensing models, *IEEE J. Oceanic. Eng.*, 14(2), 149-157, 1989.

Angle	σ_{HH}	σ_{HV}	σ_{VV}	$Re(\sigma_{hhvv})$	$Im(\sigma_{hhvv})$
37 degree	4.343×10^{-3}	5.616×10^{-4}	5.876×10^{-3}	4.239×10^{-3}	-1.788×10^{-4}
40 degree	3.861×10^{-3}	5.033×10^{-4}	5.665×10^{-3}	3.963×10^{-3}	-1.776×10^{-4}
43 degree	3.392×10^{-3}	4.458×10^{-4}	5.460×10^{-3}	3.688×10^{-3}	-1.713×10^{-4}
46 degree	2.962×10^{-3}	3.899×10^{-4}	5.265×10^{-3}	3.417×10^{-3}	-1.603×10^{-4}
49 degree	2.576×10^{-3}	3.362×10^{-4}	5.078×10^{-3}	3.151×10^{-3}	-1.452×10^{-4}

Table 1a. Normalization constants of the training data at C band.

Angle	σ_{HH}	σ_{HV}	σ_{VV}	$Re(\sigma_{hhvv})$	$Im(\sigma_{hhvv})$
37 degree	7.695×10^{-4}	1.163×10^{-4}	1.442×10^{-3}	7.819×10^{-4}	-3.291×10^{-5}
40 degree	6.205×10^{-4}	1.055×10^{-4}	1.191×10^{-3}	6.089×10^{-4}	-3.368×10^{-5}
43 degree	5.051×10^{-4}	9.476×10^{-5}	9.889×10^{-4}	4.790×10^{-4}	-3.358×10^{-5}
46 degree	4.128×10^{-4}	8.393×10^{-5}	8.268×10^{-4}	3.808×10^{-4}	-3.262×10^{-5}
49 degree	3.368×10^{-4}	7.325×10^{-5}	6.959×10^{-4}	3.054×10^{-4}	-3.086×10^{-5}

Table 1b. Normalization constants of the training data at L band.

Figure Captions

Figure 1. Polarimetric SAR scene used in this study. (Scene 1372: Beaufort Sea three frequency power image acquired at 73°2.9'N, 112°17.1 'W at 1720GMT on March 11, 1988.)

Figure 2. (a) K_a band (KRMS) scanning radiometer image of the same scene collected approximately 10 minutes ahead of the overflight; (b) Brightness temperature of the ice in the four leads.

Figure 3. Configuration of layered scattering model with description of ice properties of the layers and tile interfaces.

Figure 4. Model calculated polarimetric signature for different thicknesses. (a) C-band, (b) L-band.

Figure 5. Comparisons of the C-band polarimetric observations with model calculations. (a) Backscatter coefficients, (b) Magnitude of correlation coefficient, and (c) Phase of correlation coefficient.

Figure 6. Comparisons of the L-band polarimetric observations with model calculations. (a) Backscatter coefficients, (b) Magnitude of correlation coefficient, and (c) Phase of correlation coefficient.

Figure 7. Comparisons of the I-band polarimetric observations with model calculations. (a) Backscatter coefficients and (b) Magnitude of correlation coefficient.

Figure 8. Comparisons of measured and calculated correlation coefficients. The solid curves are calculated from the complete composite model. The dash curves are for surface scattering with no volume scattering. (a) C band ant] (b) L band.

Figure 9. Comparisons of measured and calculated correlation coefficients. The solid curves

are calculated from the complete composite model with ellipsoidal brine inclusions. The dash curves are for spherical brine inclusions. (a) C band and (b) L band.

Figure 10. Variations in the calculated correlation coefficients due to $\pm 25\%$ change in ratios of brine correlation lengths. For each type of backscatter coefficient, the upper curve is for the increase in the correlation lengths, the lower is for the decrease, and the middle is the same as the curves plotted in Figures 3 and 4. (a) C band and (b) L band.

Figure 11. An approach to retrieve ice thickness from polarimetric SAR data.

Figure 12. Characteristics of the normalized training dataset at 40° . (a) C-band and (b) L-band.

Figure 13. Estimation errors after 70,000 iterations through the backpropagation training procedure.

Figure 14. (a) Mask for thick ice. (b) Estimated distribution of ice thickness.

Figure 15. Thickness distribution obtained with C- and L-band SAR data.

Figure 16. Average thickness as a function of incidence angle.

Figure 17. Sensitivity of retrieval process to $\pm 1\text{dB}$ of calibration error (a) C-band; (b) L-band.



Fig. 1



Fig 2a

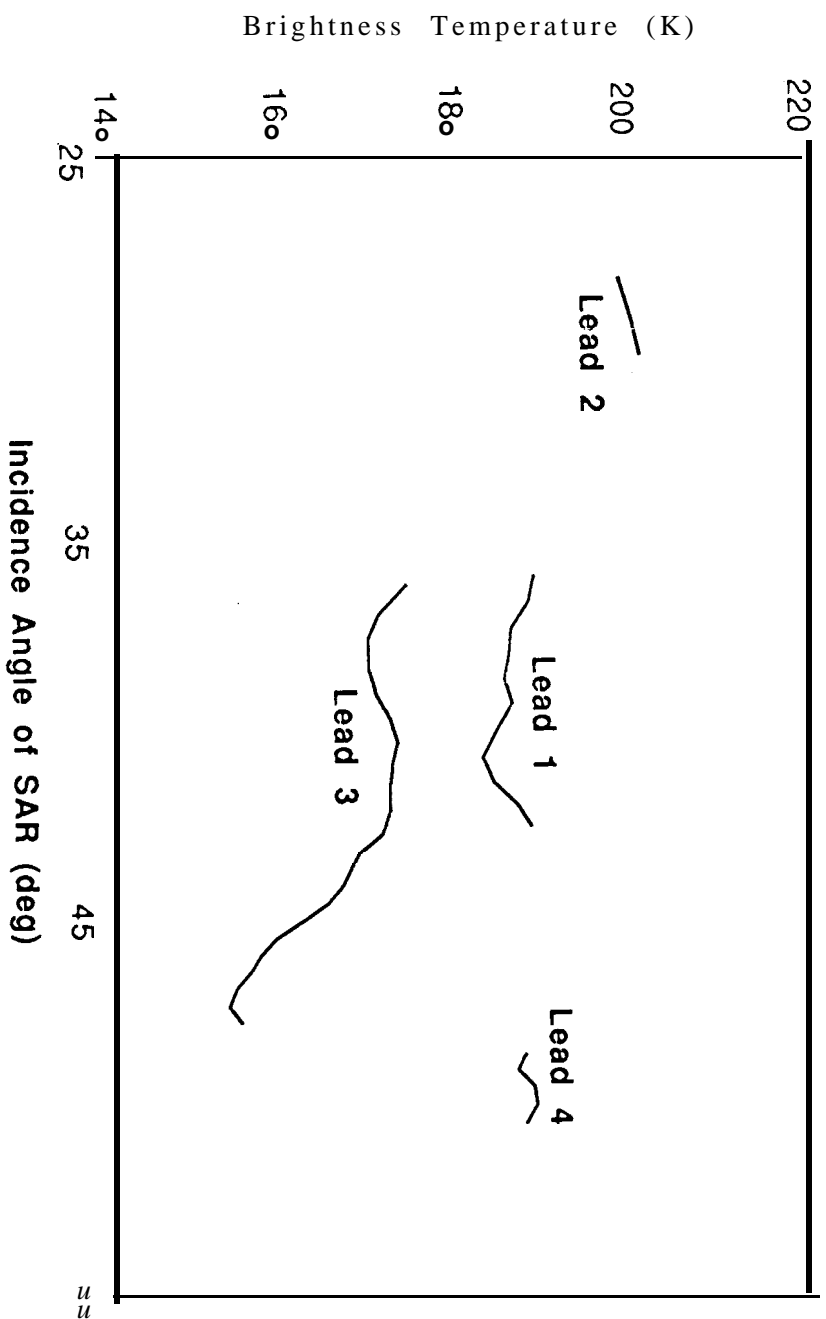
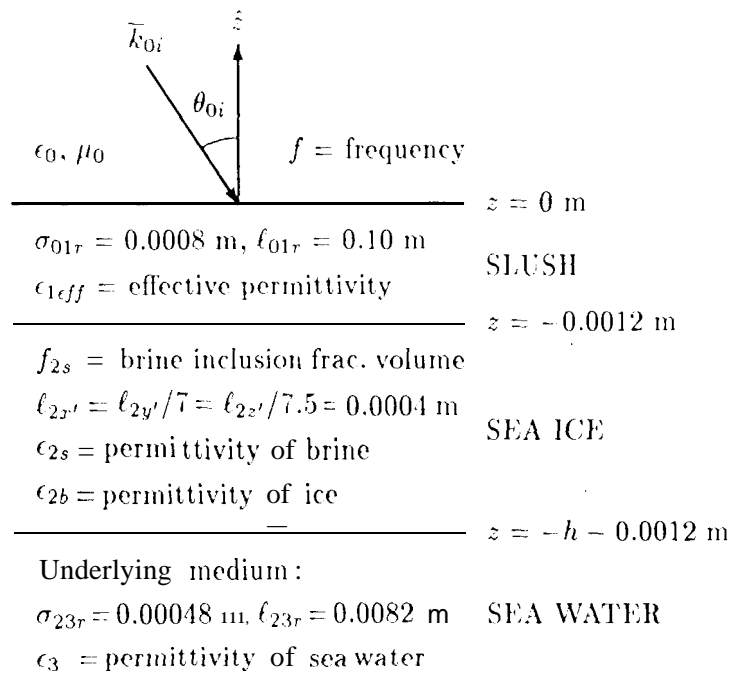
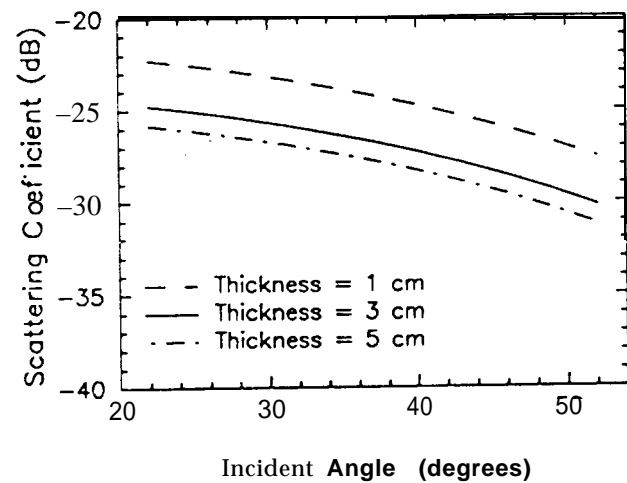
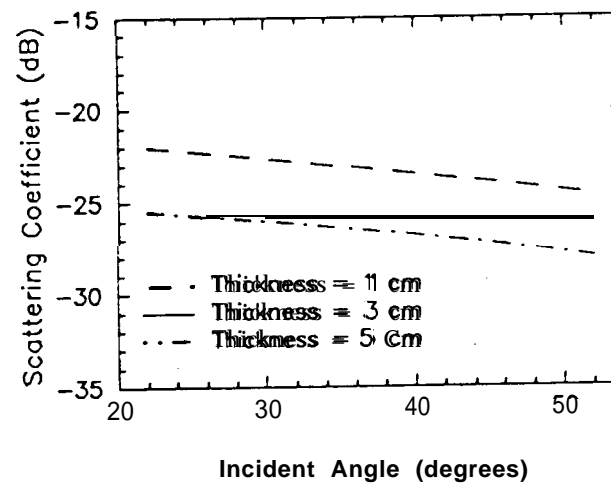
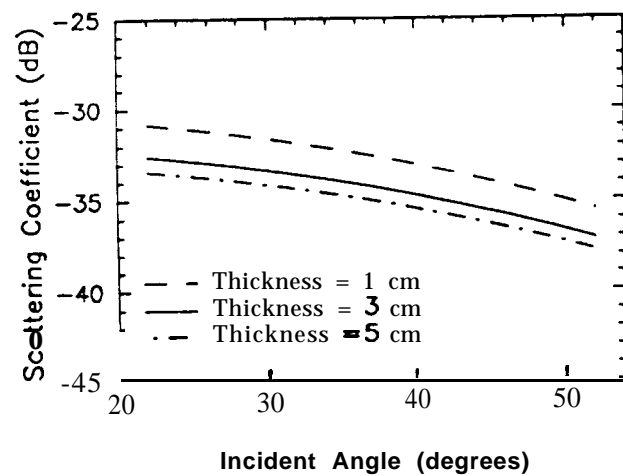
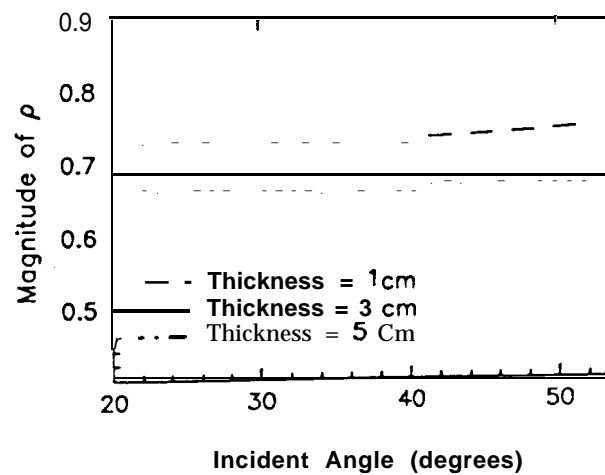
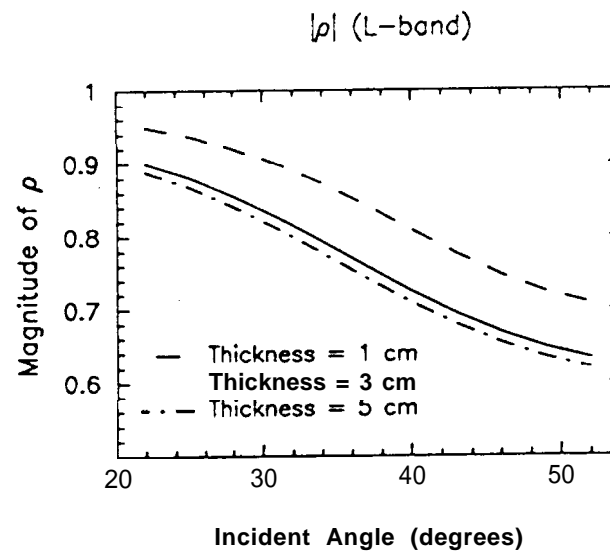
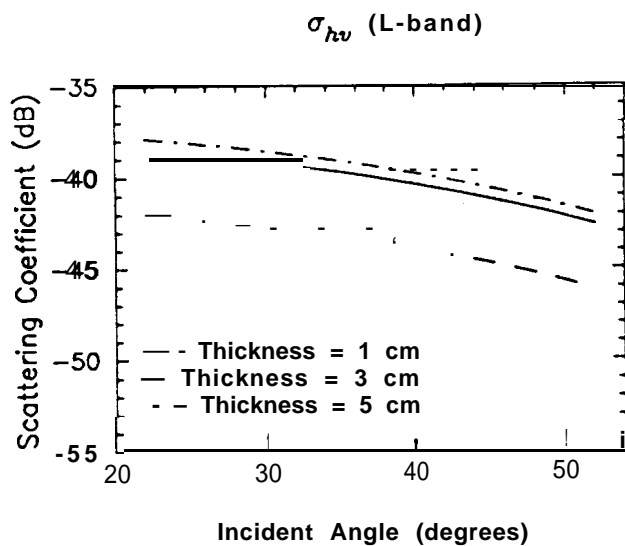
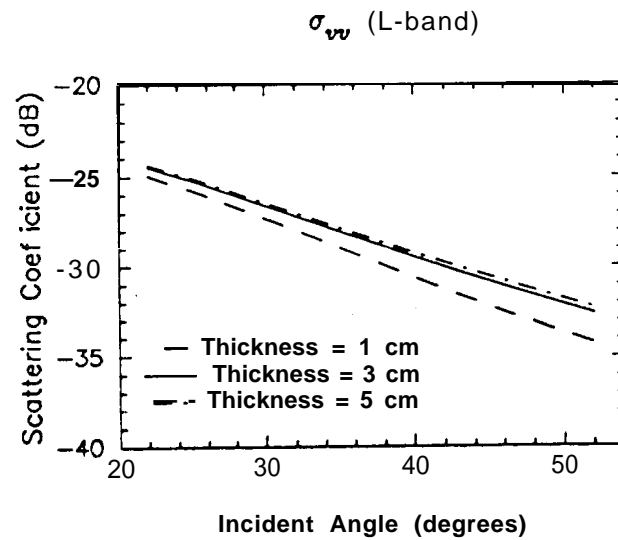
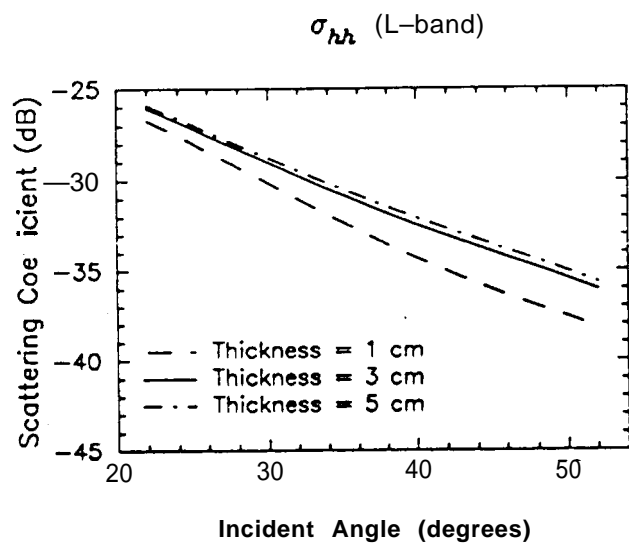


Fig 2b

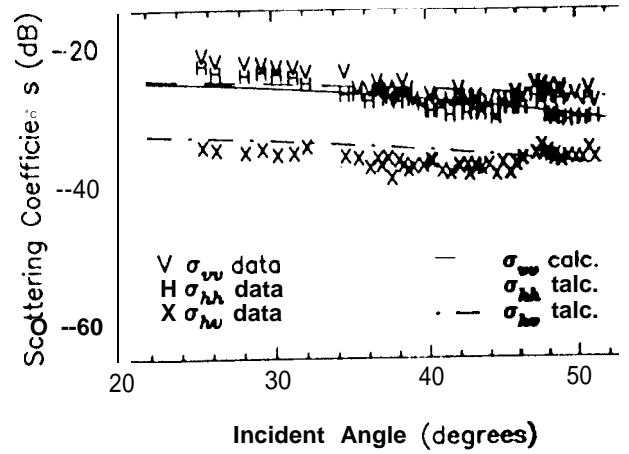


Physical parameters for thin lead ice

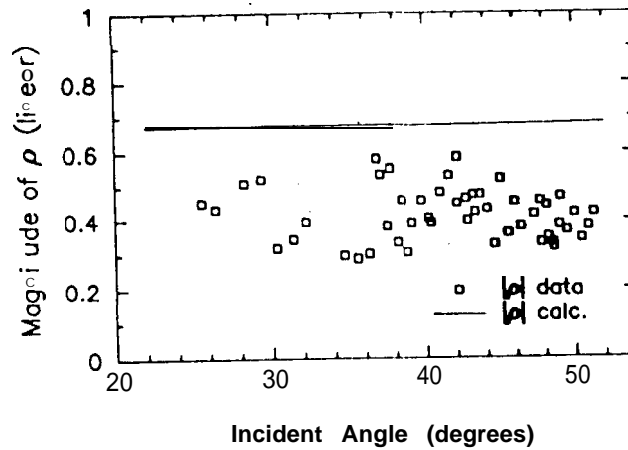
σ_{hh} (C-band) σ_{vv} (C-band) σ_{hv} (C-band) $|\rho|$ (C-band)



(a) Scattering Coefficients from 1372C



(b) Magnitude of ρ from 1372C



(c) Phase of ρ from 1372C

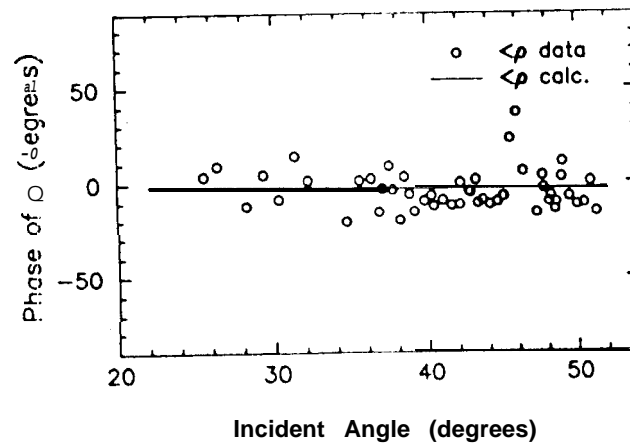
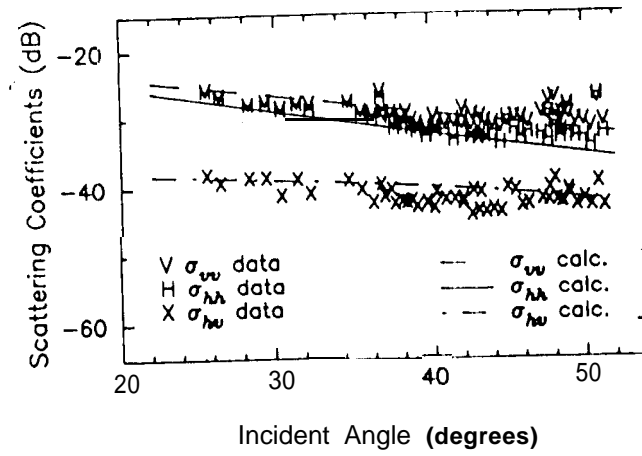
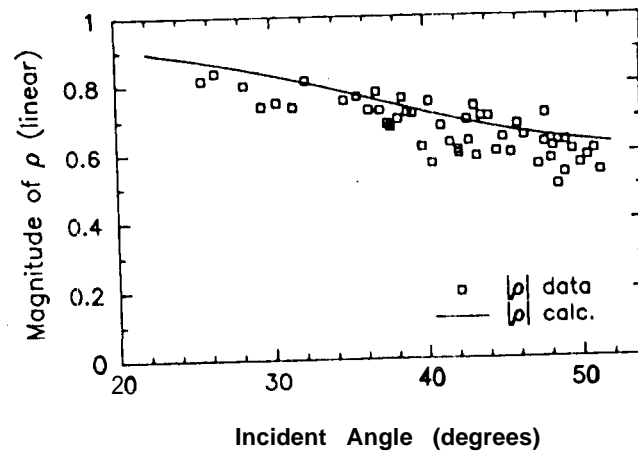


Fig 5

(a) Scattering Coefficients from 1372L



(b) Magnitude of ρ from 1372L



(c) Phase of ρ from 1372L

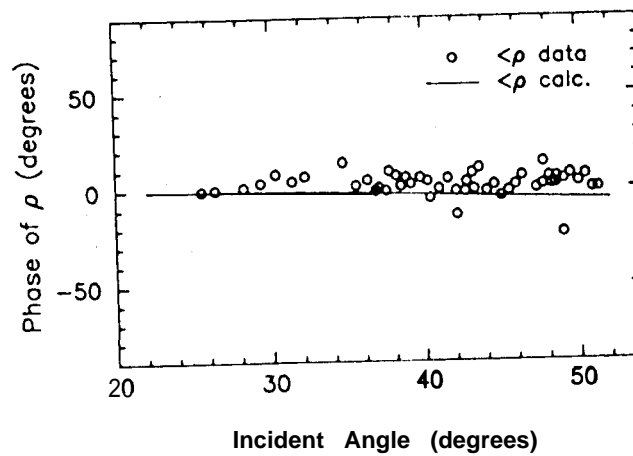
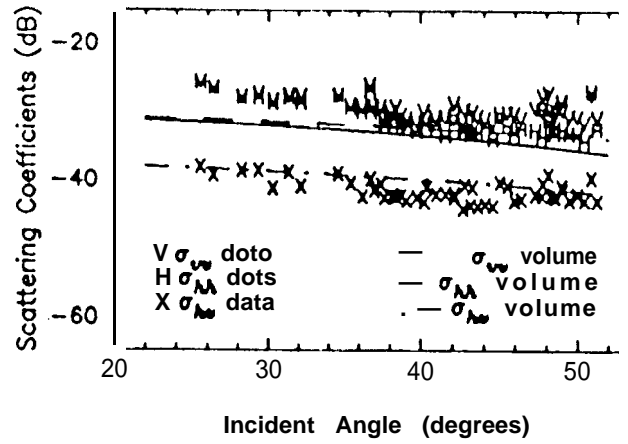


Fig. 6

(a) Scattering Coefficients from 1372L



(b) Magnitude of ρ from 1372L

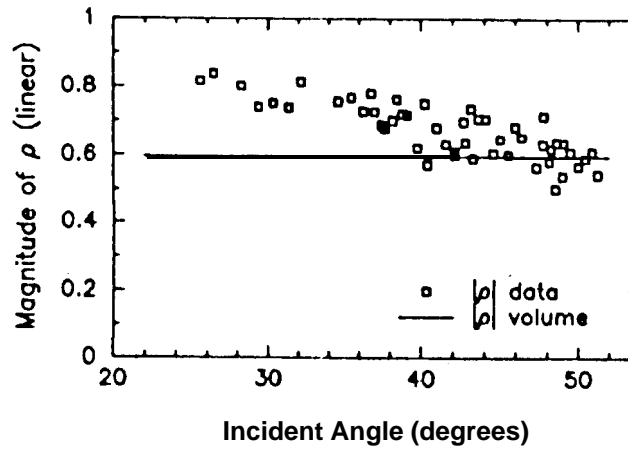
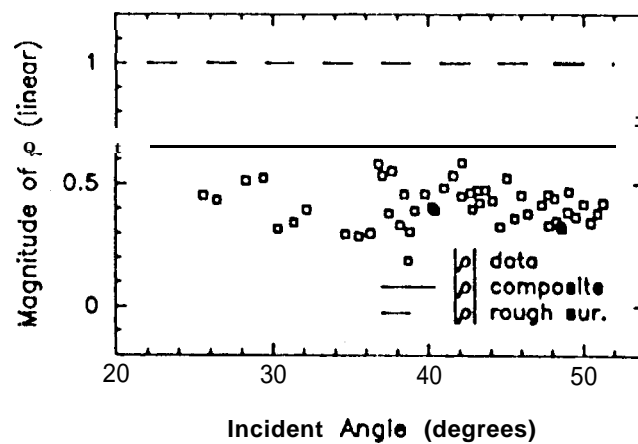


Fig. 7

(a) Magnitude of ρ from 1372C



(b) Magnitude of ρ from 1372L

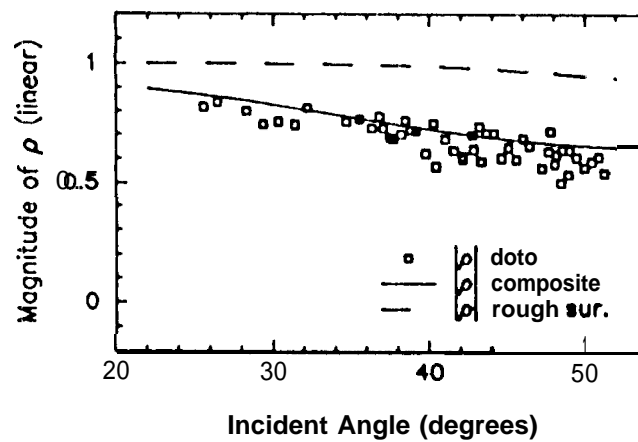


Fig. 8

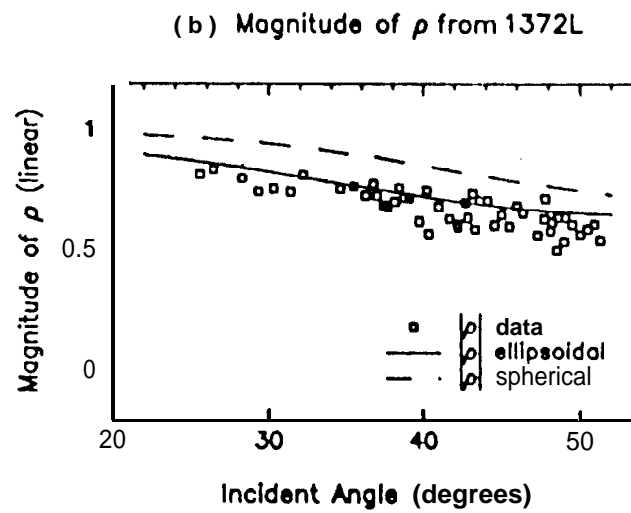
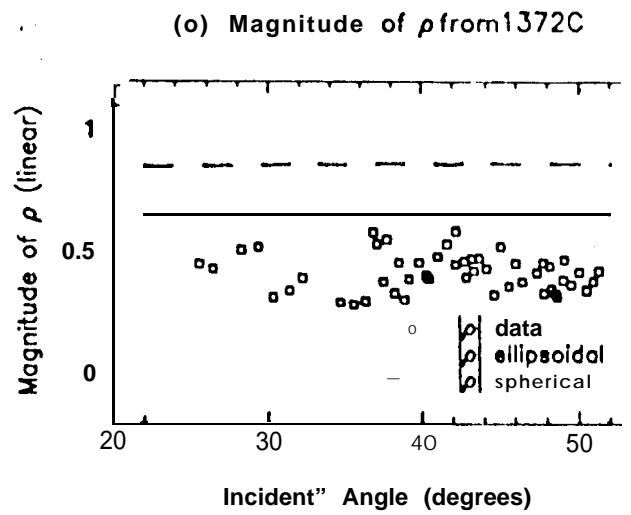
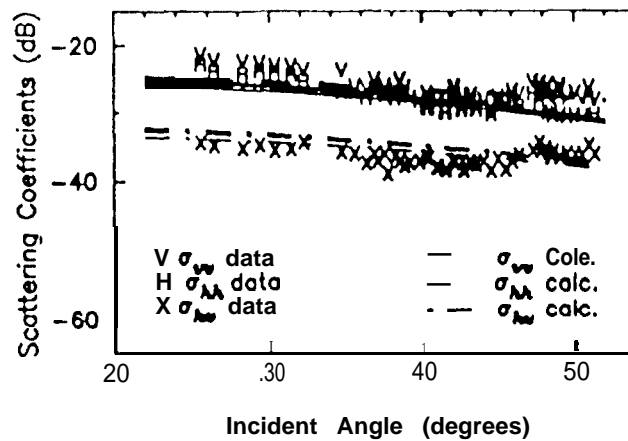


Fig. 9

(o) C Bond: Correlation Lengths in Ice



(b) L Bond: Correlation Lengths in Ice

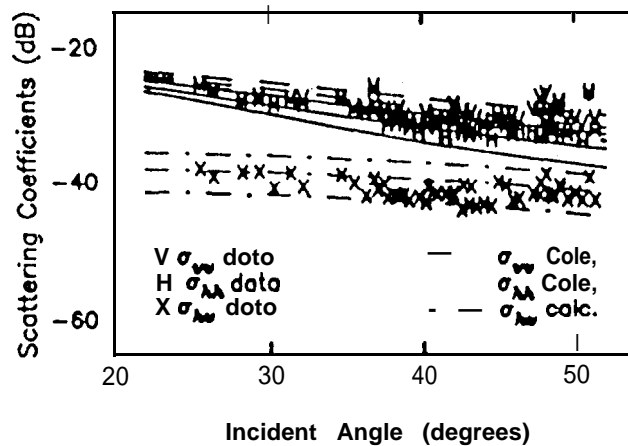


Fig. 10

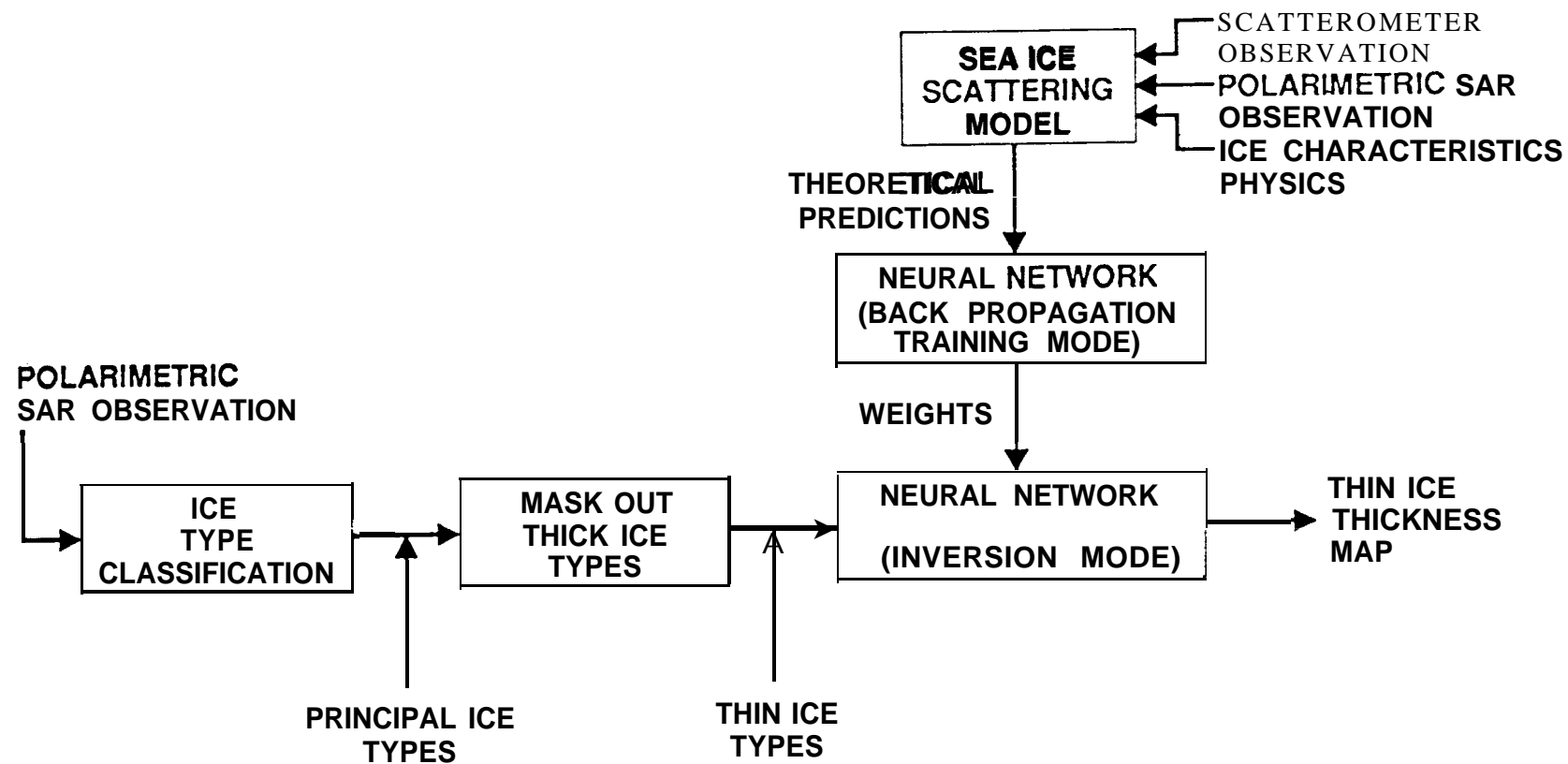
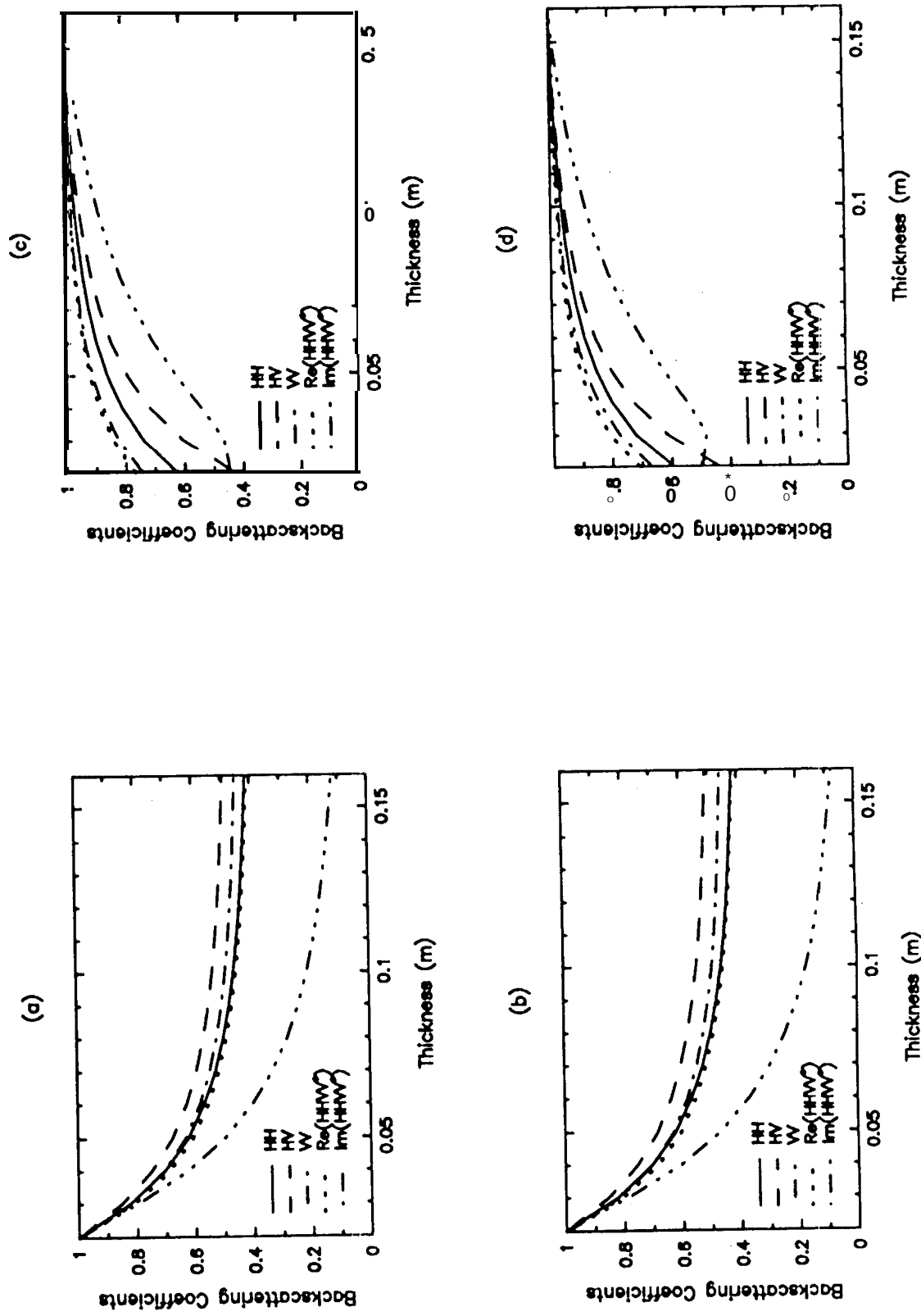
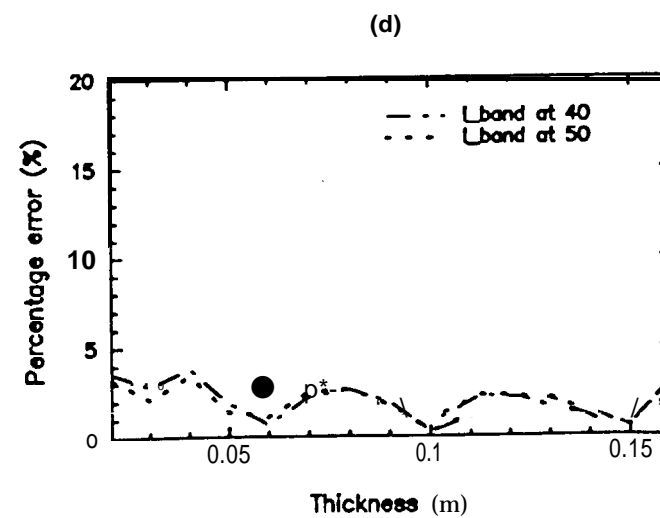
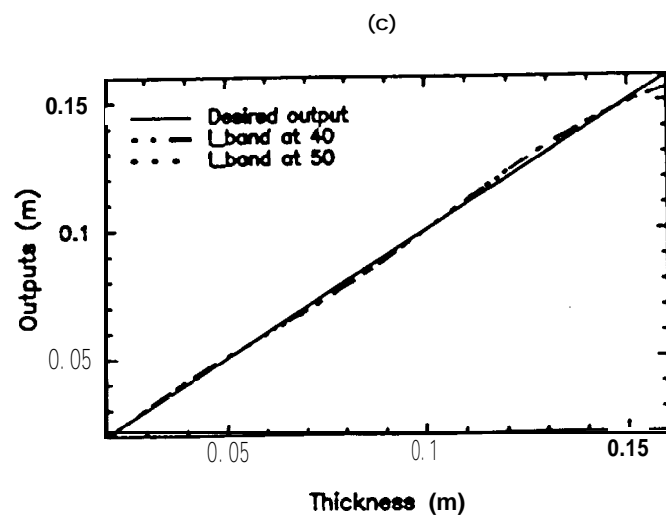
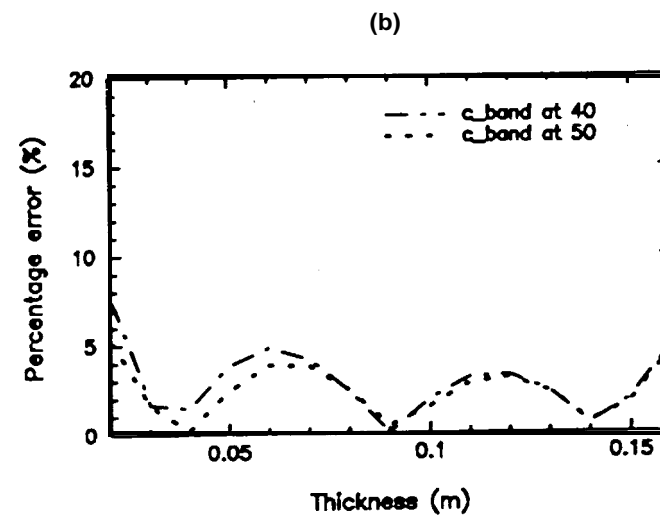
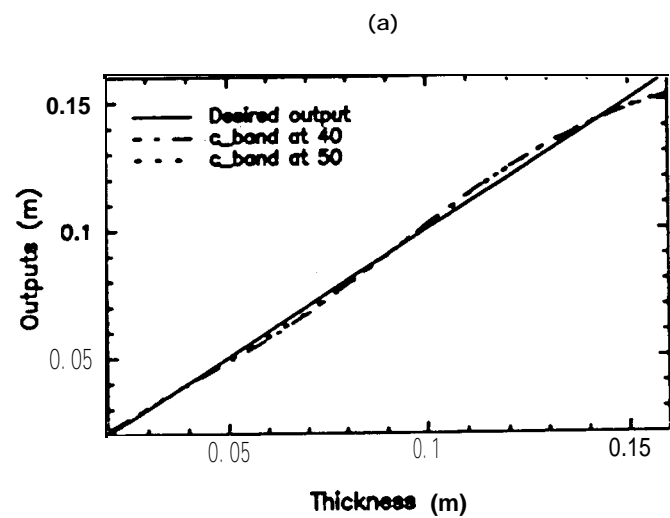


Fig. 11





POLARIMETRIC SAR DATA



DERIVED ICE THICKNESS

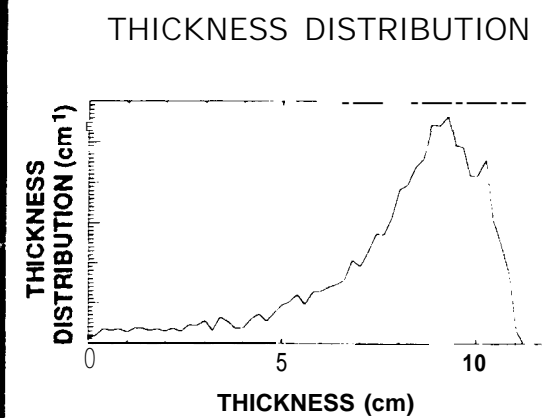


Fig. 14

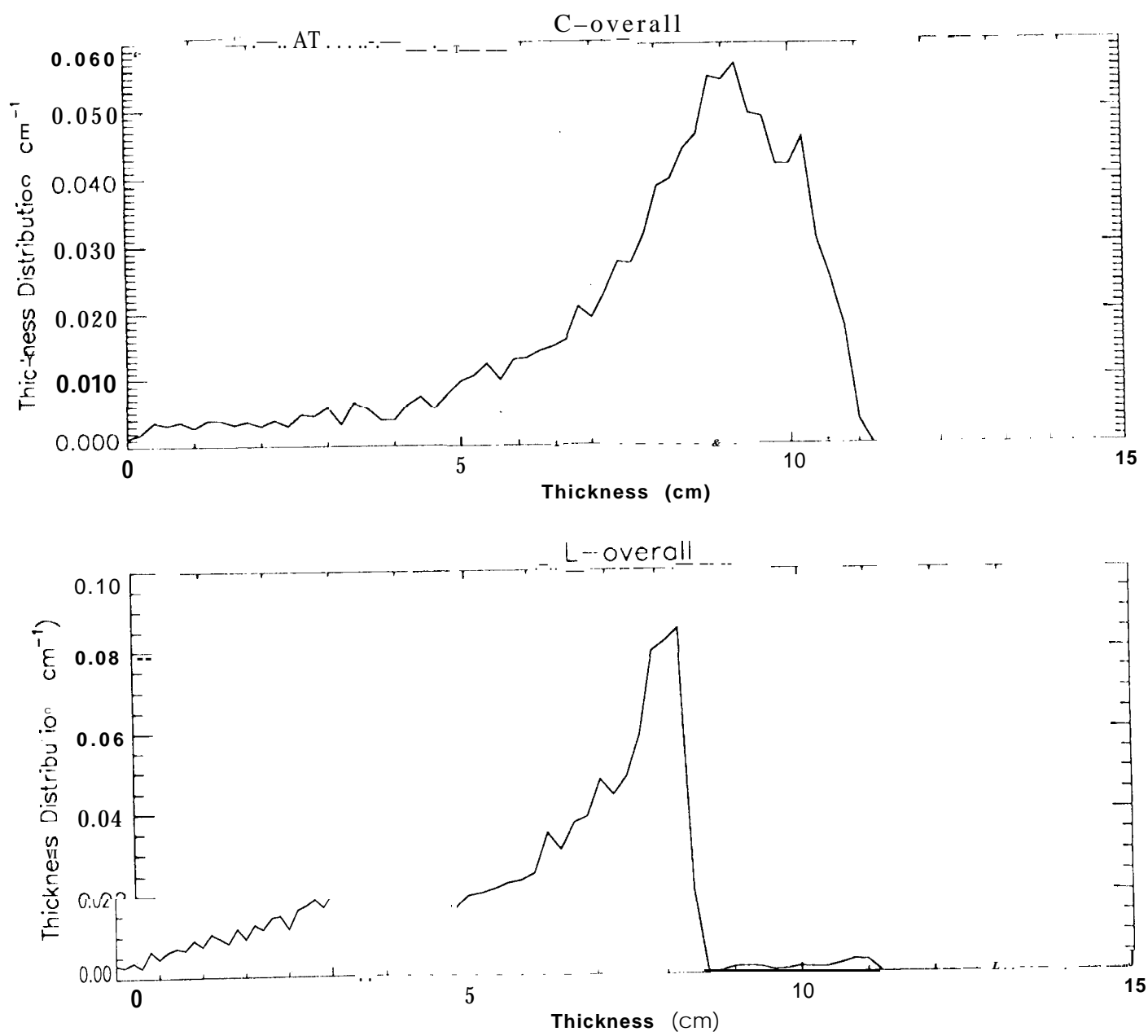


Fig. 15

HH,HV,W,Re(hhvw),Im(hhvw)

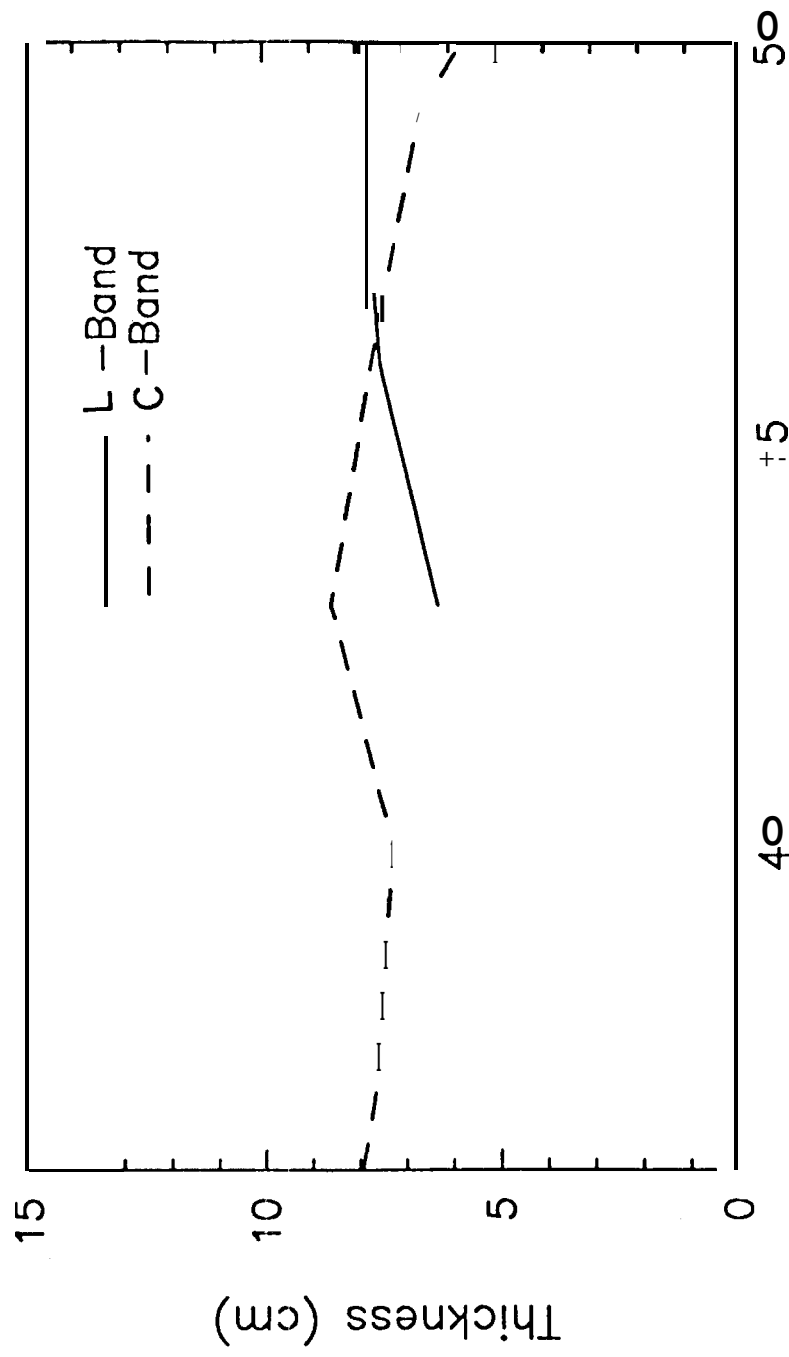


Fig. 16

HH, HV, W, Re(hhvv), Im(hhvv)

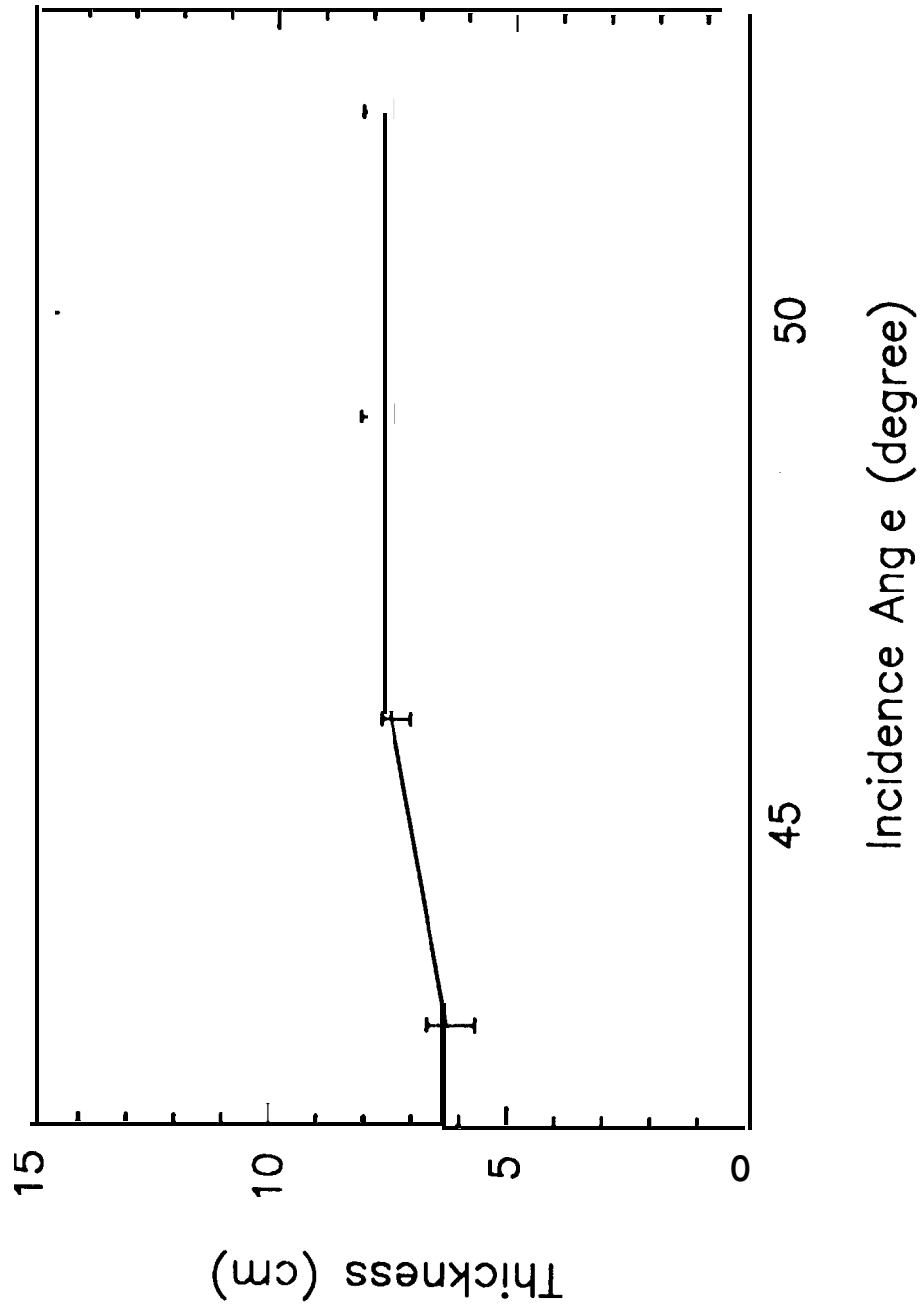
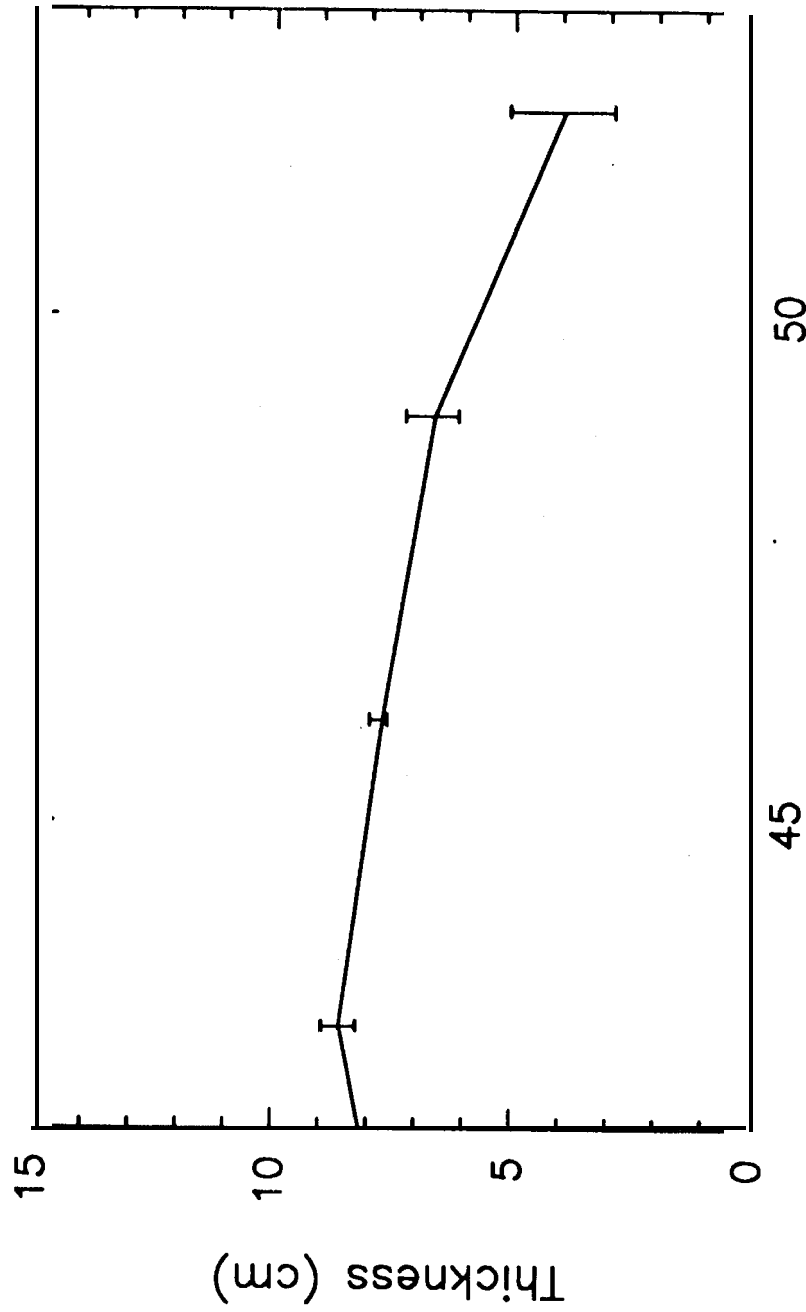


Fig. 7a

HH,HV,W,Re(hhvv),Im(hhvv)



11-9-93

ncidence Angle (degree)